



UPPSALA  
UNIVERSITET

UPTEC Q 23011

Examensarbete 30 hp

Oktober 2023

# Development of MOKE spectrometer

Sebastian Åberg

---

Civilingenjörsprogrammet i teknisk fysik med  
materialvetenskap

A large, faded watermark of the Uppsala University logo is visible in the bottom right corner of the page, partially overlapping the text.



UPPSALA  
UNIVERSITET

Development of MOKE spectrometer

Sebastian Åberg

---

### **Abstract**

The magneto-optical Kerr effect (MOKE) describes the change in polarization of light reflected from a magnetic surface. This change is proportional to the magnetization and depends on the wavelength of light. Because of these properties, MOKE has found use as a tool to probe magnetism in matter. The aim of the project is to develop an experimental setup to measure the wavelength dependence of MOKE. This is of interest as it can be used to determine the wavelength that gives the largest change in polarization to optimize measurements and provide information about the electronic structure of the sample.

Initially, the experimental setup used a laser with tunable wavelength. However, it turned out to be pulsed, which made it incompatible with the rest of the setup. Therefore, three lasers with fixed wavelengths were instead used. The setup was evaluated by measuring the Kerr rotation and hysteresis curves for three Ni samples with varying thicknesses and a TbCo sample, at three different wavelengths. The primary finding was that the setup is not suitable for spectroscopic measurements due to the inability to compare values obtained at different wavelengths. To facilitate spectroscopic measurements, a new light source with tunable wavelength is required. The setup is capable of measuring hysteresis curves.

**Teknisk-naturvetenskapliga fakulteten**

**Uppsala universitet, Utgivningsort Uppsala**

Handledare: Vassilios Kapaklis, Ämnesgranskare: Gabriella

Andersson, Examinator: Lena Klintberg

## Utveckling av MOKE spektrometer

Magnetiska material är av stort intresse från ett tekniskt perspektiv. De har funnit användning inom en lång rad av tekniska tillämpningar som sträcker sig ifrån vardagsteknik som mobiltelefoner och högtalare till generatorer i kraftverk. Den ständiga tekniska utvecklingen ställer allt högre krav på materialen som vi använder och för att möta framtidens utmaningar krävs det att vi utvecklar nya material. En viktig del i utvecklingsprocessen av nya material är att ha tillgång till mätinstrument som möjliggör analys av materialegenskaper.

Detta examensarbete går ut på att utveckla en mätuppställning som använder sig av ljus för att undersöka magnetiska egenskaper hos material. Denna undersökning baseras på att egenskaper hos ljuset förändras när det reflekteras från ett magnetiskt material. Ljusfärgen har en inverkan på denna växelverkan och syftet med mätuppställning är att undersöka detta. Från denna typ av analys får man information om beteendet hos elektronerna i materialet och vilken färg på ljuset som framkallar störst respons. Detta kan vara av intresse för tekniska tillämpningar eller andra typer av magnetiska undersökningar.

Den egenskap hos ljuset som förändras under växelverkan kallas för polarisation och den beskriver riktningen som ljusvågorna svänger. Polarisationen kan åstadkommas med en polarisator som är ett filter som enbart släpper igenom den del av ljuset som svänger i genomsläppningsriktningen. Den del av ljuset som svänger vinkelrät mot denna riktning absorberas. Figur 1 visar hur andelen ljus som passerar två polarisatorer som är placerade på varandra beror på hur deras genomsläppningsriktning är orienterade mot varandra. Allt ljus passerar när polarisatorerna är parallella som i (a) medan inget ljus passerar när de är vinkelräta mot varandra som i (c). I (b) är de orienterade med  $45^\circ$  vinkel och då släpps hälften av ljuset igenom vilket gör att det ser mer grått ut.

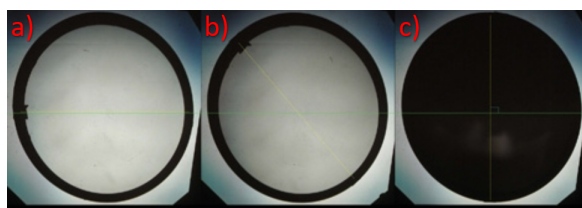


Figure 1: En bild på hur andel genomsläppt ljus beror på hur genomsläppningsriktningarna hos polarisatorerna är orienterade mot varandra. I (a) är de parallella medan de är vinkelräta i (c). I (b) är de orienterade  $45^\circ$  mot varandra. Bilden är tagen ifrån [1].

Om man långsamt vrider den övre polarisatorn så att den från början är parallell till att de är vinkelräta kommer man se att färgen förändras. Först blir det mer och mer grått tills man närmar sig läget då polarisatorerna är vinkelräta. I detta stadie blir det successivt mer mörkt. Detta fortsätter tills det blir helt svart.

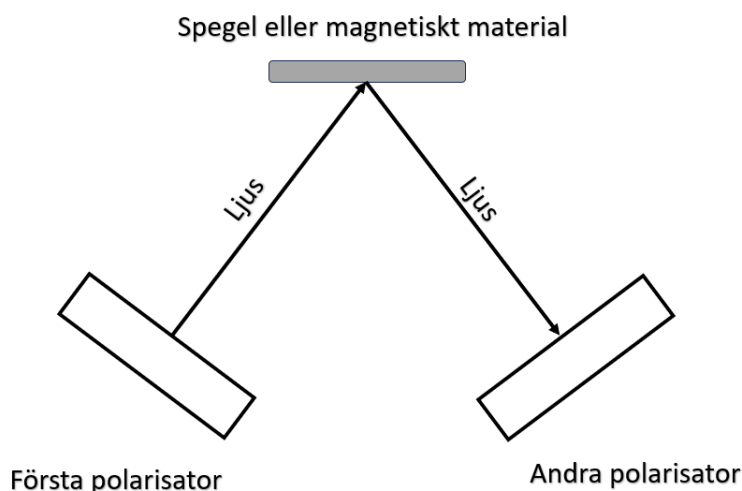


Figure 2: Illustration av en uppställning för att observera polarisationsförändringen som sker när ljus reflekteras från ett magnetiskt material.

En uppställning av två polarisatorer och en spegel enligt Figur 2 kan användas för att observera polarisationsförändringen som uppstår när ljus växelverkar med ett magnetiskt material. I denna uppställning passerar först ljuset en polarisator för att sedan reflekteras från spegeln. Det reflekterade ljuset träffar därefter den andra polarisatorn som har roterats till att den är svart som i Figur 1. Om man byter spegeln mot ett blankt magnetiskt material kommer den andra polarisatorn inte längre vara svart utan den har blivit gråaktig. Denna förändring i färg kommer från att riktningen ljuset svänger i ändras när det reflekteras från den blanka magnetiska ytan. Magnetiska egenskaper kan bestämmas från hur mycket färgen förändras. I praktiken är denna förändring i färg väldigt liten vilket gör att det oerhört svårt att se den med blotta ögat. För att kunna upptäcka och kvantifiera denna förändring behöver man införa avancerad utrustning till uppställningen.

Under arbetets gång upptäcktes det att den laser som ursprungligen skulle användas inte fungerade som det var tänkt. På grund av detta användes istället tre lasrar som skjuter ut rött, grönt och blått ljus. Detta introducerade problem som gör att det inte går att jämföra färgförändringar som var uppmätta med de olika lasrarna. Resultatet av detta är att uppställningen i dess nuvarande tillstånd inte kan användas för att undersöka ljusfärgens inverkan.

# Content

<b>1</b>	<b>Introduction</b>	<b>1</b>
1.1	Aim . . . . .	2
<b>2</b>	<b>Background</b>	<b>3</b>
2.1	Magnetism . . . . .	3
2.2	Hysteresis curves . . . . .	3
2.3	Polarization of light . . . . .	4
2.4	The magneto-optical Kerr effect . . . . .	6
2.4.1	Measuring geometries . . . . .	8
2.5	Principle of MOKE measurement . . . . .	8
2.6	Lock-In Amplifier and modulation of a light beam . . . . .	10
2.7	Photoelastic modulator . . . . .	11
2.7.1	The photoelastic effect . . . . .	12
2.7.2	Propagation in birefringent medium . . . . .	12
2.7.3	Principle of PEM . . . . .	13
2.7.4	Modulated interference . . . . .	14
<b>3</b>	<b>Experimental setup and procedures</b>	<b>15</b>
3.1	Principle of setup . . . . .	15
3.2	Setup for spectroscopy . . . . .	16
3.2.1	Light source . . . . .	18
3.3	Calibration of experimental setup . . . . .	19
3.3.1	Alignment of polarizers . . . . .	20
3.3.2	Kerr rotation calibration . . . . .	20
3.3.3	Kerr ellipticity calibration . . . . .	21
3.4	Measurement of the Kerr rotation and Kerr ellipticity . . . . .	22
3.5	Hysteresis curves . . . . .	22
<b>4</b>	<b>Method</b>	<b>23</b>
4.1	Measurement of the Kerr angles . . . . .	23
4.2	Measurement of Hysteresis curves . . . . .	24
<b>5</b>	<b>Results</b>	<b>25</b>
5.1	Calibration of Kerr rotation . . . . .	25
5.2	Kerr rotation . . . . .	25
5.3	Hysteresis curves . . . . .	27

<b>6</b>	<b>Discussion</b>	<b>30</b>
6.1	Calibration and Kerr rotation . . . . .	30
6.2	Hysteresis curves . . . . .	31
6.3	Experimental set-up . . . . .	32
<b>7</b>	<b>Conclusion</b>	<b>33</b>
<b>8</b>	<b>Future work</b>	<b>34</b>
<b>9</b>	<b>References</b>	<b>35</b>
<b>10</b>	<b>Appendix</b>	<b>38</b>

# 1 Introduction

Michael Faraday was the first to discover the interaction between light and magnetic fields in matter [2]. He found that when linearly polarized light propagates parallel to a magnetic field through a block of glass the plane of polarization undergoes a rotation. The same effect was observed for the reflection of linearly polarized light from a magnet by John Kerr. These phenomena are referred to as the Faraday effect and magneto-optical Kerr effect (MOKE). The polarization changes from these effects are proportional to the magnetization and depend on the wavelength of the light. The discovery of these effects has given rise to the field of magneto-optics (MO).

The MO effects have found use in several device applications and show promise for even more applications in the future. One of the primary applications that utilize the Faraday effect is a Faraday rotator, which is used to control the polarization of light. It is essential in devices such as optical isolators and laser systems [3]. MOKE has found wide use as a tool to probe magnetism and is utilized in data storage applications as well as in material research [4]. In these applications, MOKE is used to measure magnetic properties by analyzing the change in polarization of reflected light.

One of the advantages of MOKE compared to other magnetic measurement techniques is its high spatial resolution, which is determined by the measuring system's optics [4]. This allows it to be used for highly localized measurements by using a very focused light beam [5]. For this reason, MOKE has been utilized in the study of magnetic nanostructures. It has for example been used to study selected regions of nanowire structures and nanodot chains [6]. In addition to this, MOKE is characterized by high temporal resolution as well as high sensitivity [7, 8]. Because of this, MOKE has been used to study the dynamics of magnetism on an ultrafast time scale [6, 8].

It is from an experimental point of view, a challenge to measure magnetic properties with MOKE due to the very small change in polarization. It is, therefore, crucial to optimize the dynamic range and signal-to-noise ratio (SNR) [6]. One way to do this is to maximize the response of the sample by finding the wavelength that yields the largest change in polarization. To achieve this, one needs to measure the wavelength dependence of MOKE. It is also possible from this measurement to extract information about the electronic structure of the sample [9–11].

## **1.1 Aim**

The aim of the project is to develop a MOKE spectrometer with a laser as a light source. There have been previously developed experimental setups to do this at the Division of Materials Physics at Uppsala University that have used a white light source with a monochromator to control the wavelength of the incident light beam [12]. The advantage of using a laser instead of a white light source with a monochromator is that the optics in the system can be simplified considerably. The work in this project consists of building and calibrating the experimental setup, as well as writing software to control it.

## 2 Background

### 2.1 Magnetism

A magnetic material can be regarded as a collection of tiny current loops called magnetic moments  $\vec{\mu}$ , which arise from the motion and the spins of electrons. The magnetic behavior of a solid is described by magnetization, which is defined as the vector sum of magnetic moments divided by the volume:

$$\vec{M} = \frac{\sum \vec{\mu}}{V} \quad (1)$$

where  $\vec{M}$  is the magnetization,  $\vec{\mu}$  is the magnetic moment and  $V$  is the volume of the material. It follows from the definition that magnetization depends on the magnitude and orientation of the magnetic moments.

The application of a magnetic field  $\vec{H}$  changes the magnetization, which can be described by the magnetic susceptibility,  $\chi$ . It describes how the magnetic moments interact with each other as well as with the external magnetic field and is defined as:

$$\vec{M} = \chi \vec{H} \quad (2)$$

Depending on the value of  $\chi$  the magnetic behavior can be classified into types. In this project, there is one type of magnetic behavior that is out of interest and it is ferromagnetism. In a ferromagnetic solid, there is a strong interaction between the magnetic moment that tends to align in the same direction, which gives rise to long-range magnetic order. A ferromagnetic solid can exhibit spontaneous magnetization, i.e. non-zero magnetization in the absence of an external magnetic field.

### 2.2 Hysteresis curves

The magnetic properties of a ferromagnetic solid can be characterized by measuring how the magnetization changes as an external magnetic field is applied in a looping sequence to produce a so-called hysteresis curve. This is illustrated in Figure 3.

On the magnetization curve, there are a couple of points that are out of special interest as they correspond to material-specific magnetic properties. The saturation magnetization  $M_s$  is defined as the maximum magnetization. The remnant magnetization  $M_r$  corresponds to the points on the magnetization curve where the external magnetic field is zero. Lastly, the coercivity  $H_c$  are the points where the magnetization curve intersects the field axis.

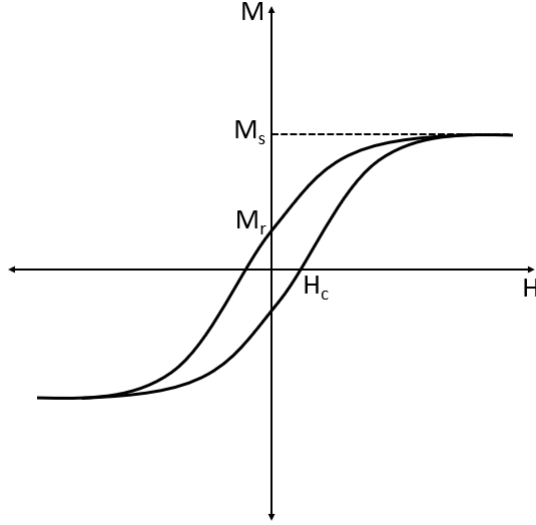


Figure 3: Hysteresis curve of a ferromagnetic material. The saturation magnetization  $M_s$ , remnant magnetization  $M_r$ , and the coercivity  $H_c$  are defined in text above.

### 2.3 Polarization of light

Light can in many situations be described as a transverse electromagnetic wave. The transverse nature of light requires that the direction of the electric field vector  $\vec{E}$  is specified over time and this is referred to as polarization [13].

A plane electromagnetic wave propagating in the  $z$ -direction can be described by [13]:

$$\vec{E} = E_x \cos(kz - \omega t)\hat{i} + E_y \cos(kz - \omega t + \delta)\hat{j} \quad (3)$$

where  $\omega$  is the angular frequency,  $k$  is the wave number and  $\delta$  is the phase shift between the  $x$  and  $y$  components. Alternatively, the electric field is described as the real part of the complex exponential function, due to the simplicity of doing computations [13]:

$$\vec{E} = \text{Re}[(E_x\hat{i} + E_y e^{i\delta}\hat{j})e^{i(kz - \omega t)}] \quad (4)$$

where  $E_x$ ,  $E_y$  and  $\delta$  are real valued.  $\text{Re}[\ ]$  in equation (4) is generally omitted and it is implied that the real part represents the electric field. Light polarization can be divided into three types: linear, circular, and elliptical. The type of polarization is determined by the values of  $E_x$ ,  $E_y$ , and  $\delta$  [14]. A way to visualize light polarization is to plot the values of  $E_x$  versus  $E_y$  for one period, which is illustrated for linear polarization in Figure 4.

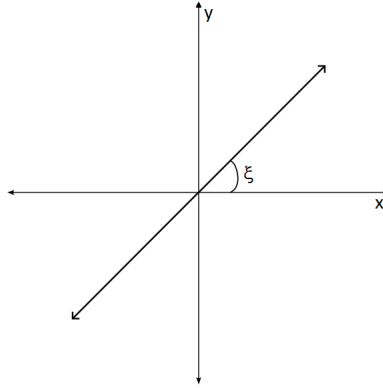


Figure 4: Illustration of linearly polarized light. The angle  $\xi$  describes the orientation of the plane of polarization with respect to the  $x$ -axis.

Linear polarization occur when  $\delta = 0$  or  $\delta = \pi$  [14]. The angle  $\xi$  in Figure 4 is determined by the relative amplitudes of  $E_x$  and  $E_y$ .

Light is circularly polarized when  $E_x = E_y$  and the phase shift is either  $\delta = \frac{\pi}{2}$  or  $\delta = \frac{3\pi}{2}$  [14]. The value of  $\delta$  determines the rotation direction of the electric field vector, which is referred to as the handedness. If  $\delta = \frac{\pi}{2}$ , the electric field vector rotates counterclockwise when viewed from the positive  $z$ -axis, which is referred to as right-handed circular polarization (RHCP). When  $\delta = \frac{3\pi}{2}$ , the electric field vector rotates clockwise, which is referred to as left-handed circular polarization (LHCP). RHCP and LHCP are illustrated in Figure 5.

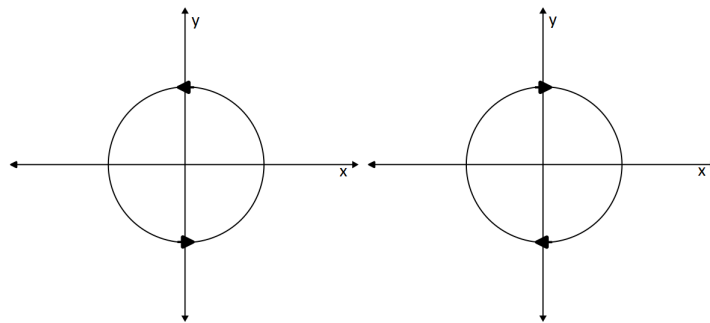


Figure 5: Illustration of RHCP light to the left and LHCP light to the right. The arrows indicate the rotation direction of the electric field vector as seen from the positive  $z$ -axis.

Elliptical polarization occurs when the conditions for linear and circular polarization are not met [14] and is illustrated in Figure 6. This ellipse can be described by two angles  $\theta$  and  $\zeta$  [3]. The angle  $\theta$  describes the tilt of the major semi-axis  $a$  with respect to the  $x$ -axis and is called the azimuth [14]. While  $\zeta$  is called the ellipticity and is defined from the ratio of the semi-minor and semi-major axes, where  $\tan(\zeta) = \frac{b}{a}$ . The sign of the ellipticity determines the handedness. When  $\zeta$  is positive the ellipse is right-handed, and if  $\zeta$  is negative the ellipse is left-handed.

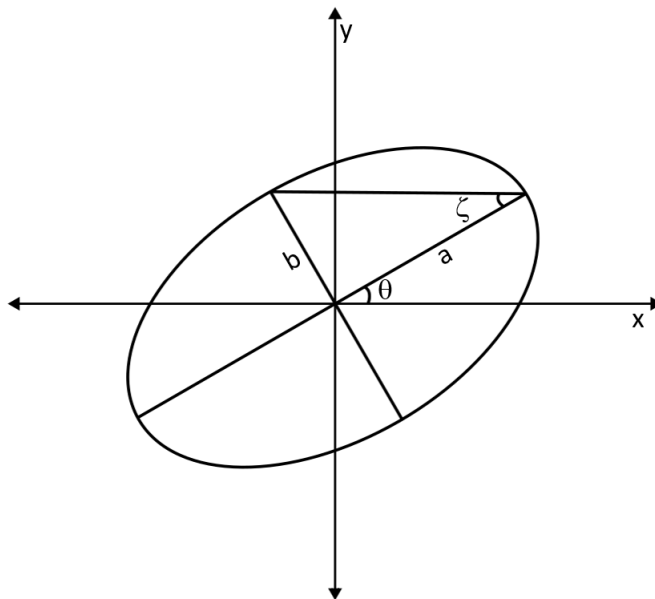


Figure 6: Illustration of elliptical polarization. The ellipse can be described by the angles  $\theta$  and  $\zeta$ , which are defined in the text above.

## 2.4 The magneto-optical Kerr effect

The magneto-optical Kerr effect (MOKE) describes the change in polarization and/or intensity of light reflected from a magnetic surface [11, 15]. Figure 7 illustrates the change in polarization when incident linearly polarized light is reflected from a magnetic surface, where the magnetization is perpendicular to the surface and parallel to the optical plane of incidence. After undergoing reflection, the light beam is elliptically polarized, which can be described by the rotation of the major axis  $\theta_K$  with respect to the plane of polarization of the incident light beam and ellipticity  $\zeta_K$ . The angles  $\theta_K$  and  $\zeta_K$  are called the Kerr rotation and Kerr ellipticity, respectively.

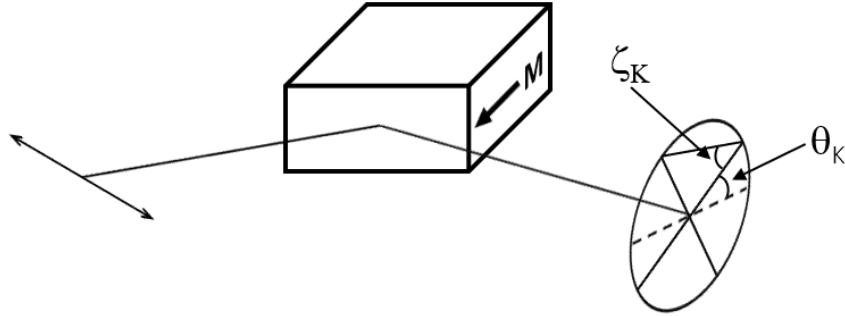


Figure 7: Illustration of the change in polarization when incident linearly polarized light is reflected from a magnetic surface. The reflected light becomes elliptically polarized, which is characterized by Kerr rotation  $\theta_K$  and Kerr ellipticity  $\zeta_K$ .

MOKE is proportional to the magnetization and dependent on the wavelength of the incoming light beam [2]. It follows that the magnitude of  $\theta_K$  and  $\zeta_K$  are determined by the absolute value of the magnetization, while their signs are determined by the direction of the magnetization at a fixed wavelength. The wavelength dependence of Kerr angles is more complicated and is shown in Figure 8 for a 90 nm thick Ni film at saturation magnetization.

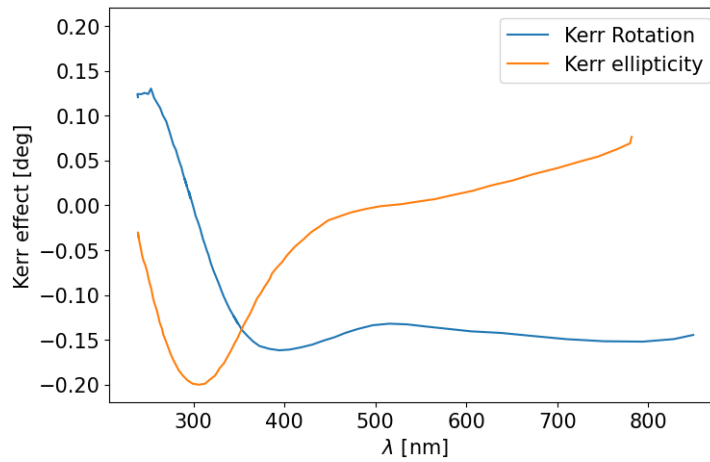


Figure 8: The wavelength dependence of MOKE for a 90 nm thick Ni film measured at saturation magnetization using polar MOKE geometry with an angle of incidence of  $4^\circ$ . The data is taken from Ref. [16] by Visnovsky *et al.*

For ferromagnetic transition metals (TM) such as Fe, Ni, and Co, the Kerr angles are smaller than  $1^\circ$  for visible light [2]. This usually also applies to TM compounds [17]. In some cases, the Kerr rotation exceeds  $1^\circ$  for a TM compound, and this is usually referred to as giant Kerr rotation [17].

The physical origin of MOKE is not addressed here, and readers are referred to the following sources: [2,18] for a detailed and comprehensive description. For this project, the essential aspect is that the polarization changes when light is reflected from a magnetic surface, which is described by  $\theta_K$  and  $\zeta_K$ .

### 2.4.1 Measuring geometries

Measurements of MOKE are performed in three geometries that are classified by the relative orientation of the magnetization with respect to the surface and the optical plane of incidence [6]. Polar MOKE corresponds to when the magnetization is perpendicular to the surface and parallel to the optical plane of incidence. The two other geometries are called longitudinal and transverse MOKE and correspond to when the magnetization is parallel to the surface and parallel or perpendicular to the optical plane of incidence, respectively. Transverse MOKE only changes the intensity, while longitudinal and polar MOKE also change the polarization [6]. The measurement geometries are illustrated in Figure 9.

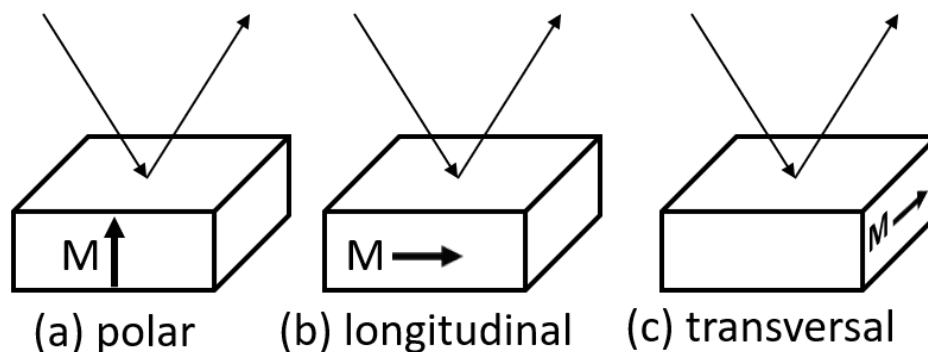


Figure 9: Illustration of the MOKE geometries: (a) polar, (b) longitudinal, and (c) transversal.

## 2.5 Principle of MOKE measurement

MOKE measurements can be performed with a wide range of different experimental setups [8]. Figure 10 illustrates one experimental setup to measure MOKE, which also forms the basis for the setup used in this project.

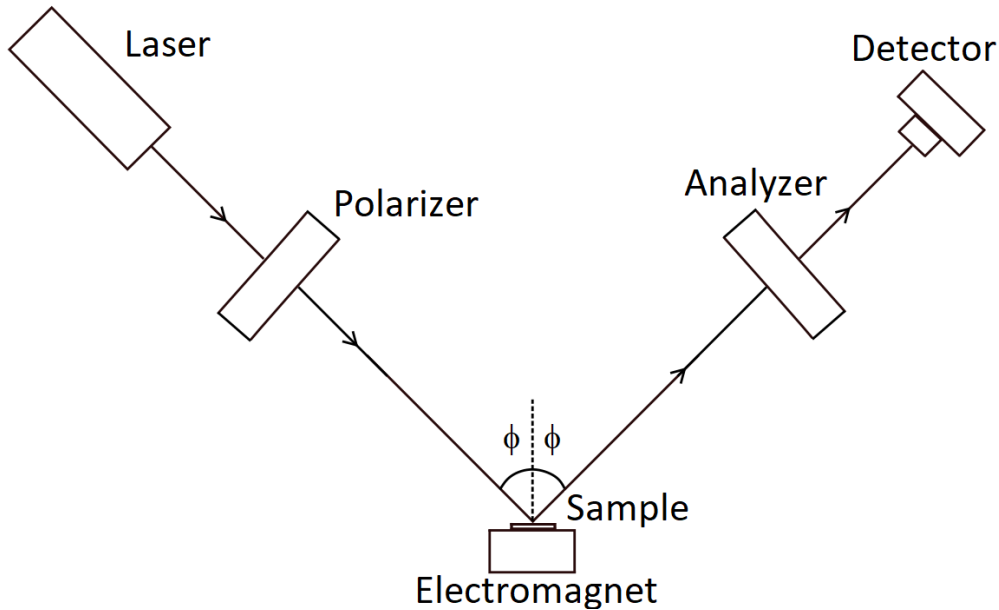


Figure 10: Schematic of an experimental setup to measure MOKE. The angle of incidence is  $\phi$ .

In this setup, the light source is a laser that produces a well-collimated light beam that propagates through a polarizer, which sets the initial polarization. The light beam then impinges upon the sample, which is mounted on an electromagnet that is used to magnetize the sample. Upon reflection, the polarization of the light beam becomes elliptical with Kerr rotation  $\theta_K$  and Kerr ellipticity  $\zeta_K$ . The reflected light beam propagates through a second polarizer, called an analyzer, that transforms the change in polarization into a change in intensity, which is measured with a detector. This change in intensity is proportional to the magnetization of the sample and in principle depends on both the Kerr rotation and Kerr ellipticity. However, in practice the change in intensity from the Kerr ellipticity is neglectable.

The Kerr rotation  $\theta_K$  can be determined by placing a mirror in the sample position and rotating the analyzer while keeping the polarizer fixed until the intensity reaches a minimum. This angle on the analyzer is referred to as the point of extinction (POX) and is denoted by  $\pi$ . When the mirror is replaced with a sample that is subjected to a static magnetic field, the intensity is no longer at a minimum. The angle that the analyzer must rotate to restore minimum intensity is the Kerr rotation,  $\theta_K$  [5]. An alternative way to determine the Kerr rotation, which also eliminated non-magnetic contributions to the change in polarization, is to determine the POX for two statically applied magnetic fields in opposite directions.

The Kerr rotation can then be determined from the difference in POX [12]:

$$\theta_K = \frac{\pi^+ - \pi^-}{2} = \frac{\theta_K + \alpha - (-\theta_K + \alpha)}{2} \quad (5)$$

where  $\pi^+$  refers to the POX of the original field direction,  $\pi^-$  to the POX of the opposite field direction, and  $\alpha$  to the non-magnetic contribution to the change in polarization. This approach also eliminates the need to use a mirror.

It is also possible to determine the Kerr ellipticity  $\zeta_k$  by introducing a wave-plate between the sample and analyzer [5]. It transforms the elliptically polarized light into linearly polarized light that is oriented at an angle  $\zeta_K$  [5]. The Kerr ellipticity is then determinable in the same way as described for the Kerr rotation.

The Kerr angles are small which results in small changes in intensity that are difficult to distinguish from background noise. This makes it difficult to accurately determine POX. It is possible to improve the signal-to-noise (SNR) by modulating the light beam and using a Lock-In Amplifier (LIA).

## 2.6 Lock-In Amplifier and modulation of a light beam

A Lock-In Amplifier (LIA) is a tool used to measure specific frequency components of a signal. It can be distinguished from the rest of the signal by the use of phase-sensitive detection, where the signal component is singled out by using a reference signal at the same frequency [19]. The reference signal is either generated internally or supplied by an external reference source. Components of the signal at other frequencies than the reference signal, such as noise, are rejected and do not affect the measurement [19]. The output from an LIA is the amplitude of the frequency component and the phase shift with respect to the reference signal. Figure 11 illustrates the input and output of a LIA.

The change in intensity with the setup in Figure 10 is constant and cannot be detected with an LIA. However, if the intensity is periodic with a specific frequency, an LIA can be used to distinguish the signal from the background noise, and this can be accomplished by modulating the light beam. Modulation is the process of altering one or more properties of a light beam such as frequency, amplitude, phase, or polarization.

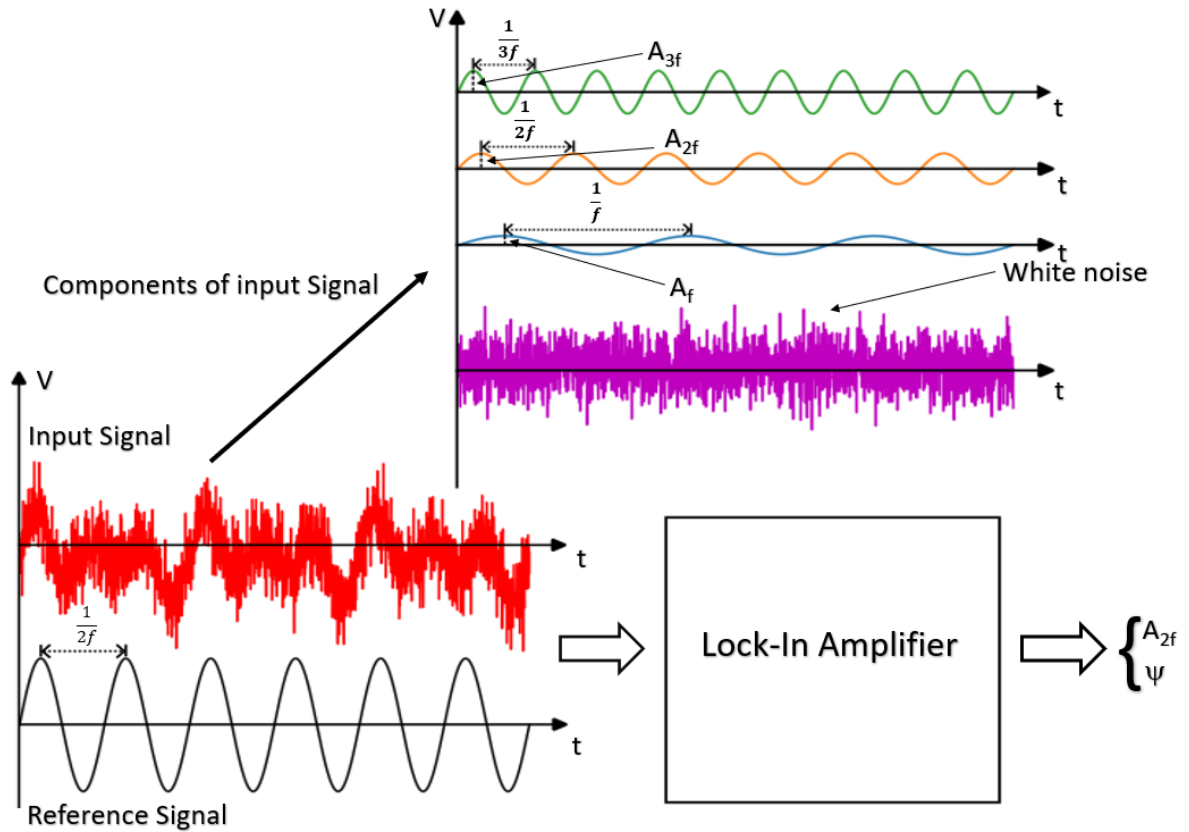


Figure 11: Illustration of the input and output of a Lock-In Amplifier. The input is a signal consisting of frequency components ranging from  $1f$  to  $3f$  and white noise. The reference signal has a frequency of  $2f$ . The output is the amplitude of the  $2f$  component  $A_{2f}$  and the phase shift  $\Psi$  with respect to the reference signal.

## 2.7 Photoelastic modulator

A light beam can be modulated with several different techniques. In this project, the light beam is modulated with a photoelastic modulator (PEM). It has found use in a wide range of applications such as amplitude modulation, polarimetry, and ellipsometry [20]. The advantage of modulating the light beam in this way is that the Kerr angles can be determined simultaneously.

In this section, the working principle of a PEM is covered, while the subsequent sections delve into the application of a PEM to determine the Kerr angles. Before the working principle is covered, a brief overview of the photoelastic effect and the propagation of polarized light through a birefringent medium is first given.

### 2.7.1 The photoelastic effect

The photoelastic effect describes the change in optical properties when a material is subjected to mechanical stress [21]. Figure 12 demonstrates the photoelastic effect, where the application of mechanical stress on an optically isotropic material introduced elastic deformation, which causes the refractive index to vary in the  $x$  and  $y$  directions. This difference in refractive index is proportional to the applied mechanical stress. When the stress is removed the material returns to being optically isotropic.

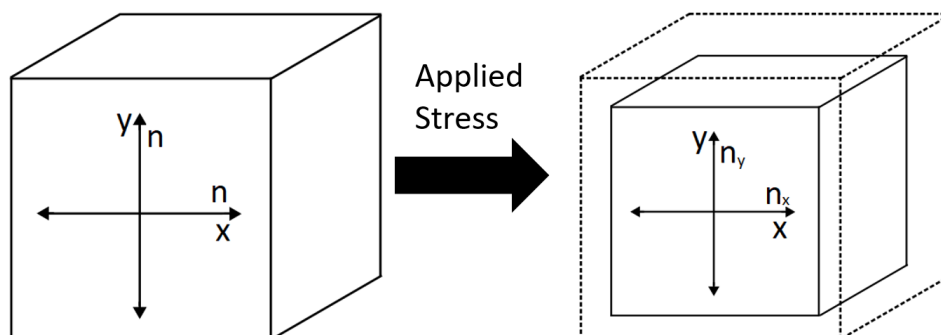


Figure 12: Illustration of the photoelastic effect where the application of mechanical stress causes a difference in refractive index.

### 2.7.2 Propagation in birefringent medium

When polarized light encounters a transparent material with different refractive index in the  $x$  and  $y$  directions, it splits into two linearly polarized light beams along these directions that propagate at different velocities [21]. The recombination of these light beams after traversing through the material introduced a phase shift, which changes the polarization, and can be calculated with the following equation:

$$\delta = \frac{\omega L}{c}(n_x - n_y) \quad (6)$$

where  $\delta$  is the phase shift,  $L$  is the thickness of the material,  $c$  is the speed of light in vacuum and  $n_{x,y}$  is the refractive index in the  $x,y$  direction. Figure 13 illustrates the change in polarization for incident linearly polarized light.

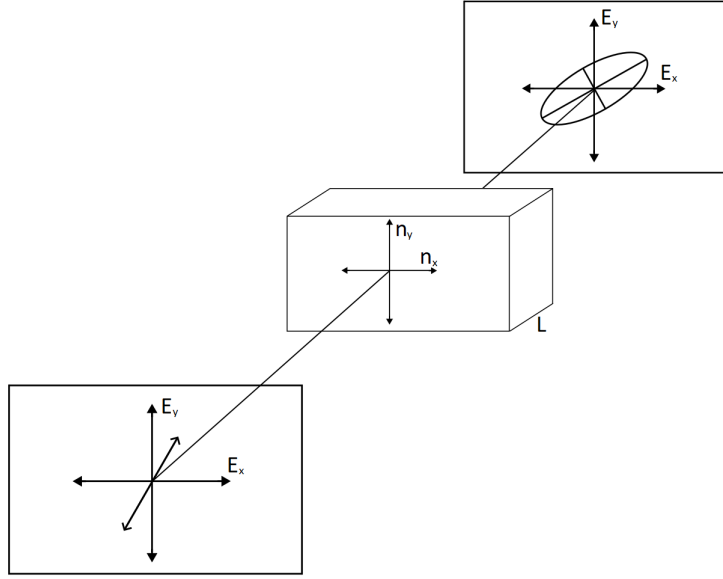


Figure 13: The effect on incident linearly polarized light as it propagates through a birefringent transparent medium. The polarization of the transmitted light changes and in general becomes elliptical.

### 2.7.3 Principle of PEM

A PEM is a device that uses the photoelastic effect to modulate the polarization of a light beam [20]. It consists of a transparent material, often fused silica, that is vibrated at a frequency  $f$  by a piezoelectric transducer [22]. This introduces a time-dependent difference in refractive indices  $n_x$  and  $n_y$ . The propagation of polarized light through the PEM introduces a periodic phase shift, which is described by:

$$\delta = A_0 \sin(2\pi ft) \quad (7)$$

where  $A_0$  is the maximum phase shift, and  $f$  is the frequency of the PEM. However, when the impinging light beam is linearly polarized and parallel to one of the optical axes, no phase shift is introduced.

Figure 14 illustrates the periodic phase shift and the corresponding change in polarization when linearly polarized light, oriented at  $45^\circ$  with respect to the  $x$ -axis, propagates through the PEM with  $A_0 = \frac{\pi}{2}$ . The polarization is unchanged at  $t = 0, \frac{1}{2f}$  and  $\frac{1}{f}$ , RHCP at  $t = \frac{1}{4f}$ , LHCP at  $t = \frac{3}{4f}$ , and is at other times in the period elliptically polarized.

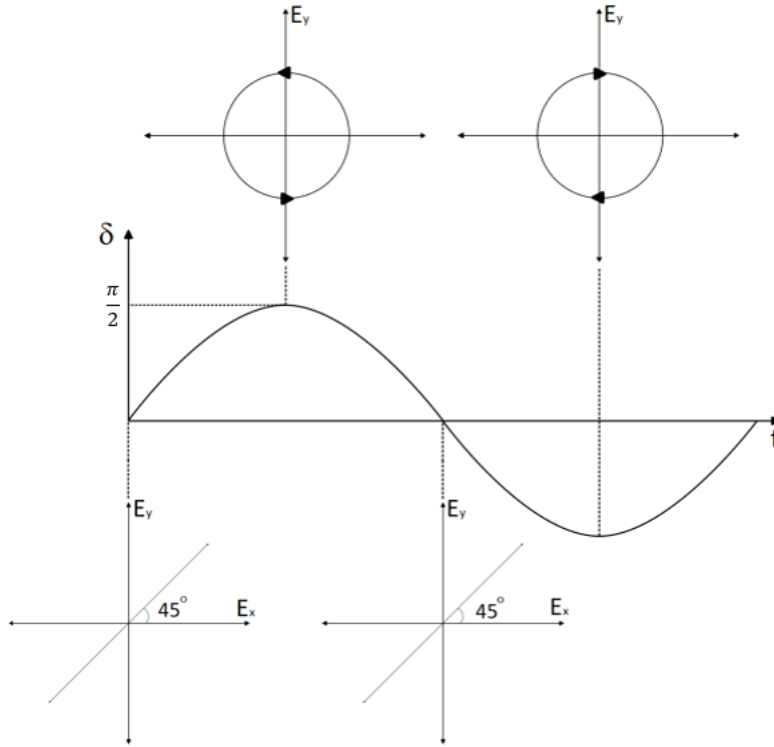


Figure 14: The time-dependent change in polarization of incident linearly polarized light oriented at  $45^\circ$  with respect to the  $x$ -axis of the PEM.

#### 2.7.4 Modulated interference

When a laser is used in combination with a PEM an effect known as modulated interference can occur. This effect arises from interference between the primary and secondary beams that emerge from reflections between the surfaces of the PEM, which are in relative motion at the modulation frequency,  $f$  [20]. The result of this is that the intensity of the transmitted light beam is amplitude modulated at the PEM frequency and its harmonics [20]. In other words, the presence of modulated interference gives rise to spurious signals at the modulation frequency and its harmonics.

### 3 Experimental setup and procedures

#### 3.1 Principle of setup

Figure 15 illustrates the experimental setup used in this project. The introduction of a PEM, two LIAs, and a multimeter (MM) to the setup shown previously allows for the simultaneous determination of the Kerr angles.

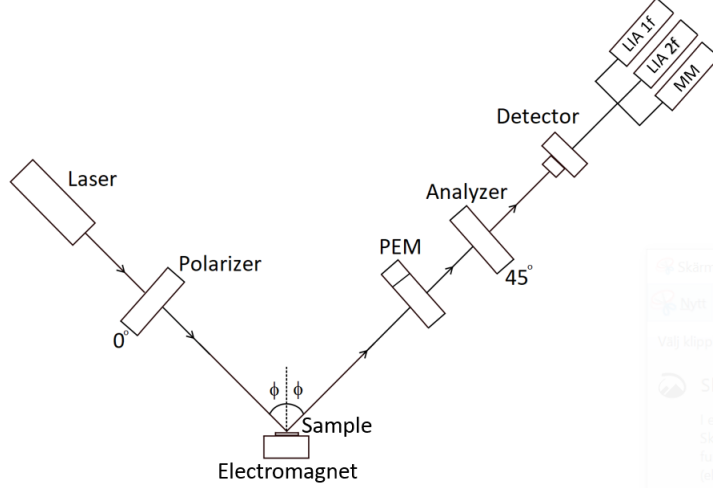


Figure 15: Illustration of the experimental setup used in this project.

In this configuration, the polarizer is oriented at  $0^\circ$  and the analyzer is oriented at  $45^\circ$  with respect to the  $x$ -axis of the PEM. When the light beam is reflected from the sample it passes through the PEM and the analyzer. A detector connected to two LIAs and an MM is used to measure the intensity of the light beam, which is described by [23]:

$$I(t) = I_0[1 + 2\theta_K J_0(A_0) - 4\zeta_K J_1(A_0) \sin(2\pi ft) + 4\theta_K J_2(A_0) \cos(2 \cdot 2\pi ft)] \quad (8)$$

where  $J_n$  is the  $n$ :th Bessel function,  $A_0$  is the maximum phase shift,  $\theta_K$  is the Kerr rotation,  $\zeta_K$  is the Kerr ellipticity, and  $f$  is the frequency of the PEM. The intensity can be divided into two DC and two AC components with frequencies  $1f$  and  $2f$ . The DC term  $2\theta_K J_0(A_0)$  is neglectable for either or both of the following two reasons: 1)  $\theta_K \ll 1$ , and/or 2)  $A_0 = 2.405$ , where  $J_0(2.405) = 0$  [23]. Furthermore, the amplitudes of the  $1f$  and  $2f$  components are proportional to the Kerr ellipticity and Kerr rotation:

$$\begin{cases} V_{1f} = 4V_{DC} J_1(A_0) \zeta_K \\ V_{2f} = 4V_{DC} J_2(A_0) \theta_K \end{cases} \quad (9)$$

where  $V_{1f}$  and  $V_{2f}$  are the amplitudes of the  $1f$  and  $2f$  components, respectively. The factor  $V_{DC}$  comes from  $I_0$  and can be determined by measuring the time average of the intensity. Expressions for the Kerr angles can be determined from the ratios of  $\frac{V_{1f/2f}}{V_{DC}}$  [23]:

$$\left\{ \begin{array}{l} \zeta_K = \frac{\sqrt{2}}{4J_1(A_0)} \frac{V_{1f}}{V_{DC}} \\ \theta_K = \frac{\sqrt{2}}{4J_2(A_0)} \frac{V_{2f}}{V_{DC}} \end{array} \right. \quad (10)$$

$$\left\{ \begin{array}{l} \zeta_K = \frac{\sqrt{2}}{4J_1(A_0)} \frac{V_{1f}}{V_{DC}} \\ \theta_K = \frac{\sqrt{2}}{4J_2(A_0)} \frac{V_{2f}}{V_{DC}} \end{array} \right. \quad (11)$$

The factor  $\sqrt{2}$  arises from the  $1f$  and  $2f$  components of the intensity being measured as the root mean square (RMS) values in the LIAs. With these expressions, the Kerr angles can be determined by measuring three signals:  $V_{DC}$ ,  $V_{1f}$ , and  $V_{2f}$  with the MM and the two LIAs.

Determining the Kerr angles with a PEM is quick since they can be derived directly from the intensity. This is useful for spectroscopic measurements where the Kerr angles are measured multiple times.

### 3.2 Setup for spectroscopy

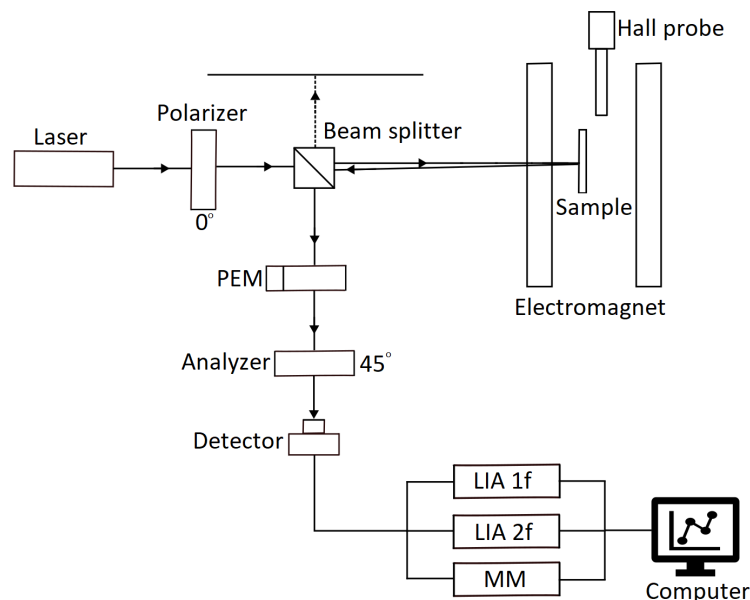


Figure 16: Schematic of the experimental set-up.

Figure 16 shows a schematic of the setup. It starts with a laser that produces a well-collimated light beam that passes through a Glan-Thompson polarizer (Thorlabs GTH10M), which is mounted on a motorized stage. Following the polarizer, the light beam propagates through a beam splitter (Thorlabs CM05-BS016), which divides the incident light beam into two beams, one that is transmitted and one that is deflected perpendicular to the right. The transmitted beam propagates into an electromagnet through a hole in the pole piece and hits the sample at normal incidence. Inside the electromagnet, the magnetic field is applied perpendicular to the surface of the sample and parallel to the optical plane of incidence, i.e. measurements are performed in polar MOKE geometry. A Hall probe (SNH34259) connected to a Lakeshore 445 Gaussmeter is used to measure the magnetic field. The electromagnet can produce a magnetic field up to approximately 1.8 T and is powered by a Kepco Power supply. A stage, that facilitates translation and rotation of the sample is used for alignment. Figure 17 shows a photo of the electromagnet, sample holder, and the Hall probe.

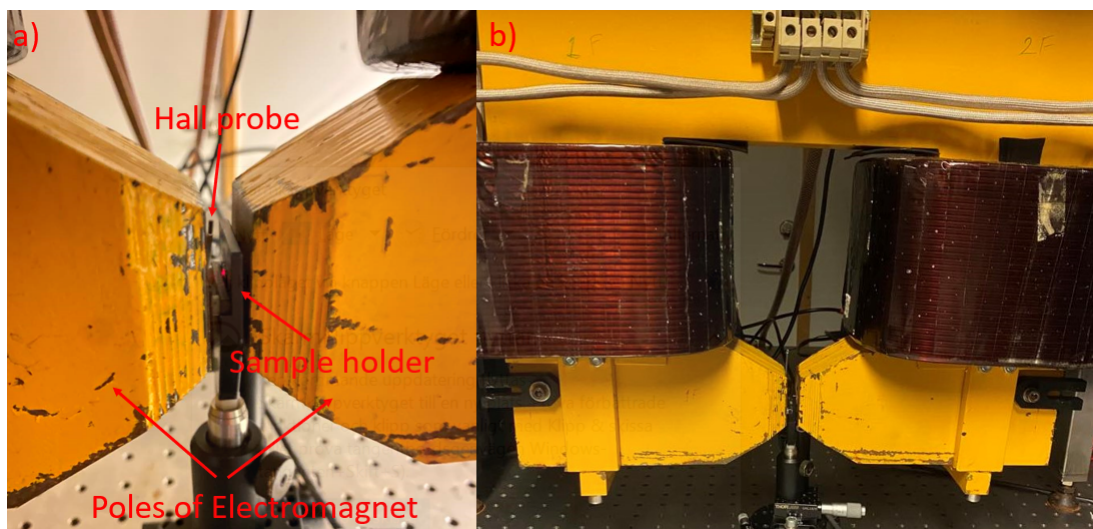


Figure 17: (a) Photo of the pole pieces, sample holder, and Hall probe. (b) Photo of the electromagnet.

The reflected light beam from the sample exits the electromagnet through the same hole as the incident light beam and hits the beam splitter. A PEM (Hinds PEM100) is used to modulate the polarization of the deflected light beam. It operates at a frequency of 50.09 kHz and is connected to a PEM controller, where the maximum phase shift is set to  $A_0 = 2.405$ . The modulated light beam propagates through an analyzer (Thorlabs GTH10M), which is mounted on a motorized stage (Thorlabs TDC001). A Si detector (Thorlabs DET100M) with a resistive

load of  $1\text{k}\Omega$  is used to detect the intensity, which is described by equation (8). Two LIAs (SR830) and an MM (Keithley 2002) are connected to the detector. These, along with the polarizer, analyzer, PEM Controller, Kepco Power supply, and Lakeshore 445 Gaussmeter are computer-controllable. LabVIEW is used to control these components and to create programs to automate calibrations as well as measurements.

The two LIAs are provided reference signals from the PEM controller at frequencies 50.09 kHz and 100.18 kHz, which corresponds to  $1f$  and  $2f$  components of the intensity. Figure 18 shows a photo of the arrangement of the laser, polarizer, beam splitter, PEM, analyzer, and detector.

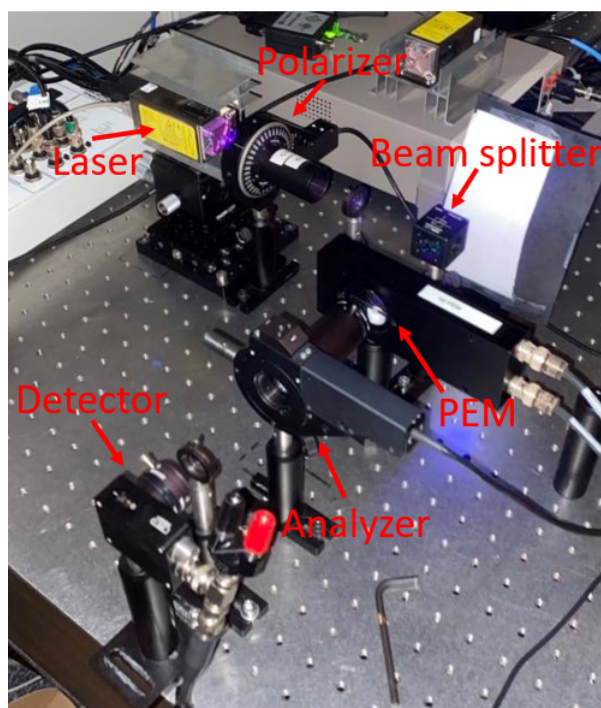


Figure 18: A photo that shows the arrangement of the laser, polarizer, beam splitter, PEM, analyzer, and detector.

### 3.2.1 Light source

Initially, the light source was a white light supercontinuum laser (Leukos Samba) used together with an acousto-optic tunable filter (Leukos Tango) to select the wavelength. Employing these, it was possible to produce laser light with wavelengths ranging from 400 to 1200 nm. However, this laser turned out to be pulsed with a nominal rate of around 30 kHz, which is shown in Figure 19.

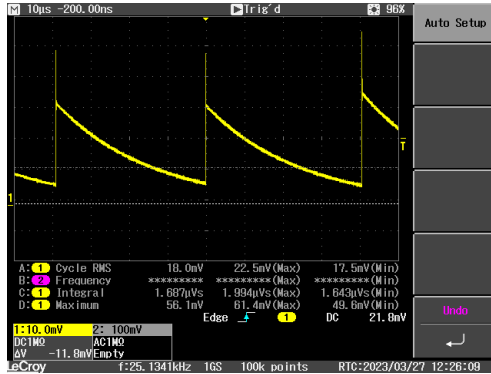


Figure 19: The voltage from Thorlabs DET100A Si detector using light from the Leukos Samba.

The self-modulated behavior of the laser introduced noise into the measurement of the  $1f$  and  $2f$  signals, which made it incompatible with the PEM. Therefore, three lasers with fixed wavelengths were instead used and these are displayed in Table 1.

Table 1: The lasers used in the experimental set-up.

Laser	Wavelength [nm]
Coherent CUBE 405-50C	408
Coherent OBIS 532-20 LS	532
Coherent CUBE 640-40C	640

### 3.3 Calibration of experimental setup

The calibration of the experimental setup consists of two parts. The first part is the alignment of the polarizer and analyzer with respect to the  $x$ -axis of the PEM. The second part is the calibration of the Kerr angles, which are determined with equations (10) and (11). However, these equations are derived under the assumption that the light beam strikes the optical components at normal incidence and that all optical components are ideal. The goal is to determine a relationship between the Kerr angles and  $\frac{V_{1f/2f}}{V_{DC}}$  that takes into account that the setup is not ideal:

$$\left\{ \begin{array}{l} \zeta_K = k_{ellip} \cdot \frac{V_{1f}}{V_{DC}} + m_{ellip} \\ \theta_K = k_{rot} \cdot \frac{V_{2f}}{V_{DC}} + m_{rot} \end{array} \right. \quad (12)$$

$$\left\{ \begin{array}{l} \zeta_K = k_{ellip} \cdot \frac{V_{1f}}{V_{DC}} + m_{ellip} \\ \theta_K = k_{rot} \cdot \frac{V_{2f}}{V_{DC}} + m_{rot} \end{array} \right. \quad (13)$$

The calibrations are performed with an aluminum mirror at the sample position, which is non-magnetic and does not alter the polarization state of the light beam during reflection. When the polarizer is oriented at  $0^\circ$  and the analyzer at  $45^\circ$  with respect to the  $x$ -axis of the PEM, the polarization of the light beam remains unchanged as it propagates through the setup. Consequently, the intensity is constant and it follows that  $V_{1f} = V_{2f} = 0$ . However, if the polarizer is oriented at an angle  $\theta$  while the analyzer is oriented at  $45^\circ$ , the intensity is described by:

$$I(t) = I_0[1 + 4\theta J_2(A_0) \cos(2 \cdot 2\pi ft)] \quad (14)$$

In this case,  $V_{2f} \neq 0$ . Note that  $V_{1f}$  is always zero because the impinging light beam upon the PEM is always linearly polarized.

### 3.3.1 Alignment of polarizers

The main challenge with the alignment of the polarizer and analyzer is that the orientation of the  $x$ -axis of the PEM is unknown with respect to the transmission axes of the polarizer and analyzer. It can be found by rotating the polarizer and analyzer, which are oriented at  $45^\circ$  with respect to each other, and measuring the change in  $V_{2f}$ . It is found when  $V_{2f} = 0$ .

This process was implemented in LabVIEW. In order to explain how the program works, two things must be addressed. Firstly, the approximate position of the  $x$ -axis was found before the program was written by manually turning the polarizer and analyzer while reading the value of  $V_{2f}$  directly from the display. Secondly, the change in  $V_{2f}$  is linear for small angles.

In the program, the polarizer and analyzer are rotated at several small angles near the  $x$ -axis, and the corresponding changes in  $V_{2f}$  are measured. A linear fit is then performed of  $V_{2f}$  versus the rotation angles of the polarizer. From the obtained slope and intercept, the angle  $\Sigma$  that corresponds to  $V_{2f} = 0$  is calculated. Lastly, the polarizer is moved to  $\Sigma$  and the analyzer is moved  $45^\circ$  relative to  $\Sigma$ .

### 3.3.2 Kerr rotation calibration

The calibration of the Kerr rotation is performed by rotating the polarizer to several small angles  $\theta$  from  $0^\circ$  while the analyzer is kept fixed at  $45^\circ$  and measuring the corresponding changes in  $\frac{V_{2f}}{V_{DC}}$ . A linear fit of  $\theta$  versus  $\frac{V_{2f}}{V_{DC}}$  gives  $k_{rot}$  and  $m_{rot}$ . This process was implemented in LabVIEW. Figure 20 shows a plot of  $\theta$  versus  $\frac{V_{2f}}{V_{DC}}$  with the linear fit.

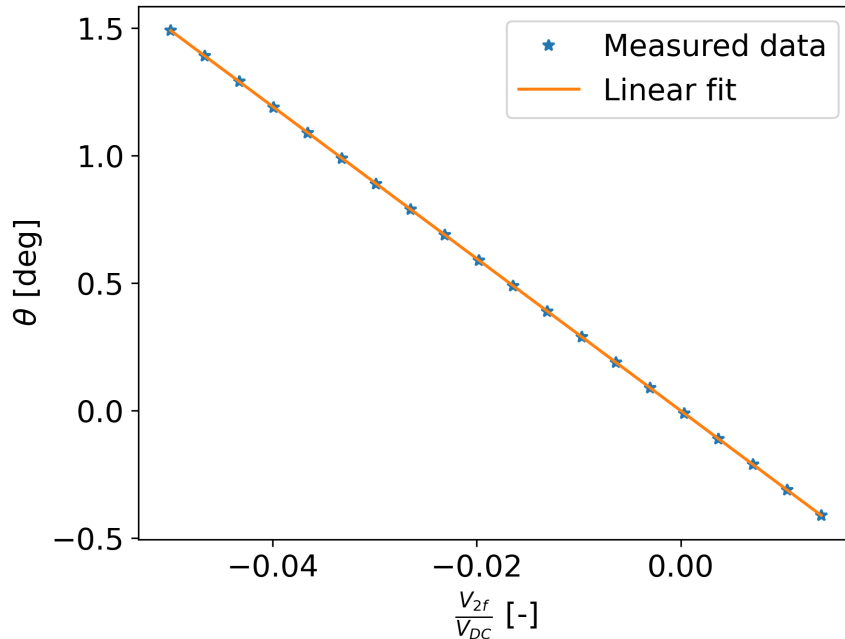


Figure 20: A plot from the calibration of the Kerr rotation that shows  $\theta$  versus  $\frac{V_{2f}}{V_{DC}}$  as well as the linear fit.

### 3.3.3 Kerr ellipticity calibration

The Kerr ellipticity can be calibrated in the same way as the Kerr rotation by measuring the change in  $\frac{V_{1f}}{V_{DC}}$  for several small ellipticities  $\zeta$ . However,  $V_{1f}$  is always zero since the light beam is always linearly polarized as it strikes the PEM. The light beam can become elliptically polarized by introducing a quarter-wave plate between the polarizer and beam splitter in Figure 16. It is an optical component used to change the polarization of the light beam and consists of a birefringent material. The thickness of the birefringent material is chosen such that a  $90^\circ$  phase shift is introduced between two orthogonal polarization components. It follows that the polarization of the transmitted light beam can be controlled by rotating the polarizer, which changes the orientation of the incident linearly polarized light beam with respect to the optical axes of the quarter-wave plate. To do this, the optical axis must be determined, which is achieved by rotating the polarizer and measuring the change in  $V_{1f}$ . The optical axis is found when  $V_{1f} = 0$ .

The calibration of the Kerr ellipticity is performed by rotating the polarizer around the optical axes of the quarter-wave plate to produce polarization states with small ellipticities  $\zeta$  and measure the changes in  $\frac{V_{1f}}{V_{DC}}$ . The linear fit of  $\zeta$  versus  $\frac{V_{1f}}{V_{DC}}$  gives  $k_{ellip}$  and  $m_{ellip}$ .

### 3.4 Measurement of the Kerr rotation and Kerr ellipticity

The measurement is performed by applying static magnetic fields in two opposite directions and measuring  $V_{1f}$ ,  $V_{2f}$ , and  $V_{DC}$ . The Kerr angles can then be determined with equations (12) and (13) for each direction. Non-magnetic contributions to the change in polarization can be eliminated by taking the difference between the obtained Kerr angles:

$$\left\{ \begin{aligned} \zeta_K &= \frac{k_{ellip}}{2} \left( \frac{V_{1f+}}{V_{DC}} - \frac{V_{1f-}}{V_{DC}} \right) = \frac{\zeta_K + \gamma - (-\zeta_K + \gamma)}{2} \end{aligned} \right. \quad (15)$$

$$\left\{ \begin{aligned} \theta_K &= \frac{k_{rot}}{2} \left( \frac{V_{2f+}}{V_{DC}} - \frac{V_{2f-}}{V_{DC}} \right) = \frac{\theta_K + \alpha - (-\theta_K + \alpha)}{2} \end{aligned} \right. \quad (16)$$

where  $\alpha$  and  $\gamma$  are the non-magnetic contributions to the change in polarization. The superscript  $+$  refers to the original field direction and  $-$  to the opposite.

This process was implemented in LabVIEW. In the program, the user specifies the magnetic field strength  $H$  and the number of times to measure the Kerr angles,  $N_{repeat}$ . The mean value and standard deviation are calculated from the repeated measurements.

### 3.5 Hysteresis curves

Hysteresis curves are measured by applying a sweeping magnetic field in a looping sequence and measuring the corresponding change in intensity. Note that the change in intensity is proportional to the magnetization and in most cases this proportionality factor is unknown. Consequently, the relative change in magnetization is only observable from the plot of the intensity versus the applied magnetic field.

For this experimental setup, two signals can be measured and these are  $V_{1f}$  and  $V_{2f}$ . The hysteresis curves are measured with a pre-written LabVIEW program designed for a longitudinal MOKE setup that does not utilize a PEM and is therefore only capable of measuring one signal at the same time.

The pre-written LabVIEW program applies a magnetic field as a triangular wave, where the maximum magnetic field strength  $H_{max}$ , sweep rate  $\frac{\Delta H}{\Delta t}$ , number of loops  $N_{loops}$ , and the number of points per loop  $N_{points}$  are set by the user. The hysteresis curve is produced by averaging the values measured in each loop.

## 4 Method

The setup was tested on three Ni films with varying thicknesses and a film of  $\text{Tb}_{18}\text{Co}_{82}$  with a buffer and cap of  $\text{AlO}_x$ . Table 2 shows the substrate material, film material, thicknesses, and sample names.

Table 2: The material, thickness, and substrate material of the samples.

Sample name	Material	Thickness [nm]	Substrate material
Ni-150	Ni	150	Si
Ni-30	Ni	30	Glass
Ni-24	Ni	24	Si
TbCo	$\text{Tb}_{0.18}\text{Co}_{0.82}$ <sup>1</sup>	20	Glass

<sup>1</sup> Glass/5nm  $\text{AlO}_x$ /20 nm  $\text{Tb}_{0.18}\text{Co}_{0.82}$ /2 nm  $\text{AlO}_x$

### 4.1 Measurement of the Kerr angles

It was found during the calibration of the Kerr rotation that  $V_{1f} \neq 0$  for all lasers in Table 1. This can be attributed to the presence of modulated interference. By adjusting the optical path of the light beam through the PEM, the noise in  $V_{1f}$  could be reduced. However, noise into  $V_{2f}$  was instead introduced. It was not possible to reduce the noise in  $V_{1f}$  and  $V_{2f}$  at the same time, which is consistent with literature [20]. A decision was made to reduce the noise in  $V_{2f}$  and only calibrate and measure the Kerr rotation due to a lack of time as the project deadline was approaching. Consequently, the calibration process for the Kerr ellipticity was not implemented.

The Kerr rotation was measured at three wavelengths: 408, 532, and 640 nm with the lasers in Table 1. At each wavelength, the laser had to be swapped, which required repositioning and adjustment of the optical components to ensure a proper beam path. Because of this, the Kerr rotation was re-calibrated at each wavelength. The intensity used for each laser varied because of the wavelength-dependent response of the detector, which is shown in the Appendix. For the Coherent CUBE 640-40, the intensity was set to 1.25 mW, while it was set to 5 mW for Coherent CUBE 405-50C. The software to control the Coherent OBIS 532-20 LS did not work. Thus, the used intensity is unknown. To maximize the MOKE signal, the measurements were performed at saturation magnetization, which for Ni is 500 mT and for TbCo is 250 mT. The parameters used in the LabVIEW program for each sample were:  $H_{max} = 900$  mT and  $N_{repeat} = 100$ .

## 4.2 Measurement of Hysteresis curves

For all the samples, hysteresis curves were measured with both the  $1f$  and  $2f$  signals at the wavelengths 408, 532, and 640 nm with the pre-written LabVIEW program described previously. In the program the parameters were set to  $H_{max} = 1000$  mT,  $\frac{\Delta H}{\Delta t} = 15$  mT/s and  $N_{loops} = 2$  for all the measurements except for Ni-30 at 408 nm, where  $H_{max} = 800$  mT.

## 5 Results

### 5.1 Calibration of Kerr rotation

The obtained calibration factors are shown in Table 3 for each wavelength.

Table 3: The calibration factor  $k_{rot}$  at wavelengths: 408, 532, and 640 nm. No uncertainties are given for  $k_{rot}$  as the  $R^2$  obtained from the linear fits are approximately 1.

Wavelength [nm]	$k_{rot}$ [deg]
640	40.205
532	28.172
408	21.041

Another calibration was performed at 640 nm, in which  $k_{rot} = 32.507$  deg. This value differs significantly from the other calibration.

### 5.2 Kerr rotation

Table 4 shows Kerr rotations obtained from the two calibrations performed at 640 nm. The result shows a small difference in Kerr rotation for Ni-24 and Ni-150, while there is a greater difference for Ni-30 and TbCo.

Table 4: Obtained Kerr rotations at 640 nm for two different calibrations. The uncertainties are estimated from the standard deviation.

	Kerr rotation [deg]			
	Ni-24	Ni-30	Ni-150	TbCo
$k_{rot} = 32.507$	$-0.162 \pm 0.001$	$-0.209 \pm 0.002$	$-0.154 \pm 0.002$	$-0.588 \pm 0.002$
$k_{rot} = 40.205$	$-0.159 \pm 0.008$	$-0.231 \pm 0.002$	$-0.150 \pm 0.003$	$-0.655 \pm 0.002$

The spectroscopic measurements of the Kerr rotation for the Ni samples are shown in Figure 21. These are compared to values obtained by Visnovsky *et al.* using polar MOKE on a 90 nm thick Ni film [16]. There is some agreement between the measured and literature values, especially for Ni-24 and Ni-150 at 532 and 640 nm. Ni-30 deviates distinctly at 532 and 640 nm but shows a better agreement at 408 nm.

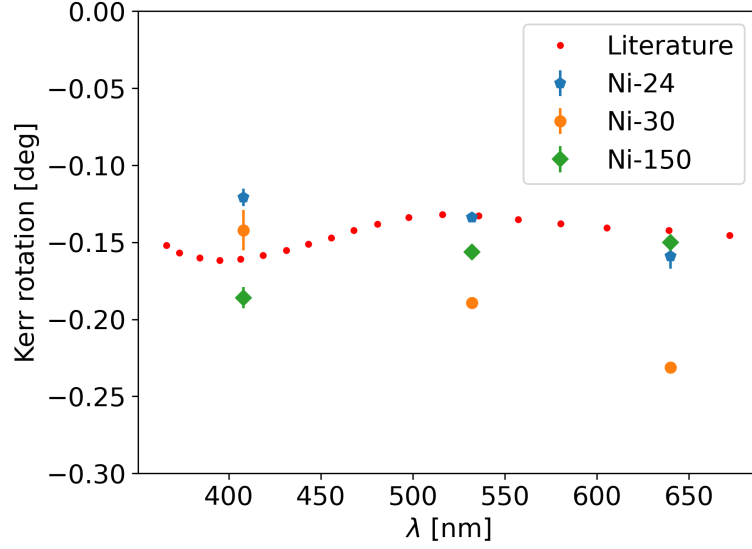


Figure 21: The obtained Kerr rotations are calculated with the calibrations factors in Table 3. The literature values are obtained by Visnovsky *et al.* in Ref. [16].

Figure 22 shows the spectroscopic measurement of TbCo, which is compared to values obtained by Ciuciulkaite *et al.* on a Tb<sub>18.4</sub>Co<sub>81.6</sub> film with a buffer and cap of Al<sub>80</sub>Zr<sub>20</sub> (Glass/3.2 nm Al<sub>80</sub>Zr<sub>20</sub>/16.5 nm Tb<sub>18.4</sub>Co<sub>81.6</sub>/2.9 nm Al<sub>80</sub>Zr<sub>20</sub>) [24]. The sign differs and there is a large difference in magnitude.

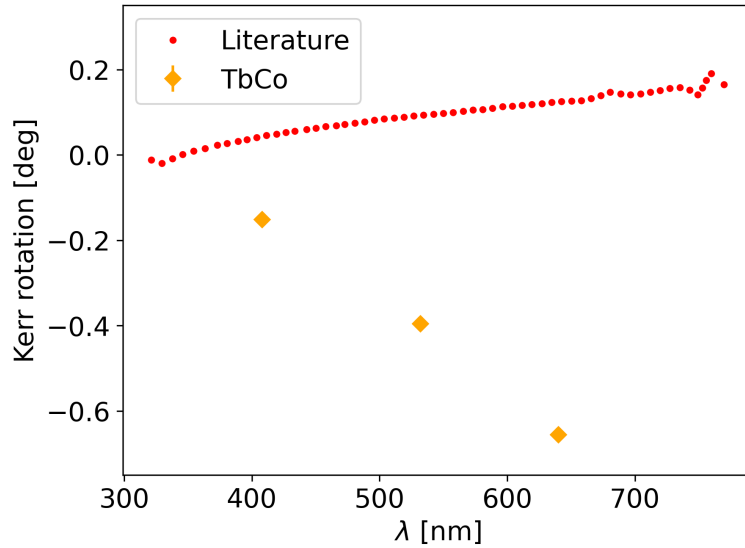


Figure 22: The obtained Kerr rotations are calculated with the calibrations factors in Table 3. The literature values are obtained by Ciuciulkaite *et al.* in Ref. [24].

### 5.3 Hysteresis curves

Figure 23 shows the hysteresis curves obtained for TbCo with the  $1f$  and  $2f$  signals. The direction differs for the curves obtained with the  $1f$  and  $2f$  signals, which shows that the Kerr angles differ in sign at these specific wavelengths.

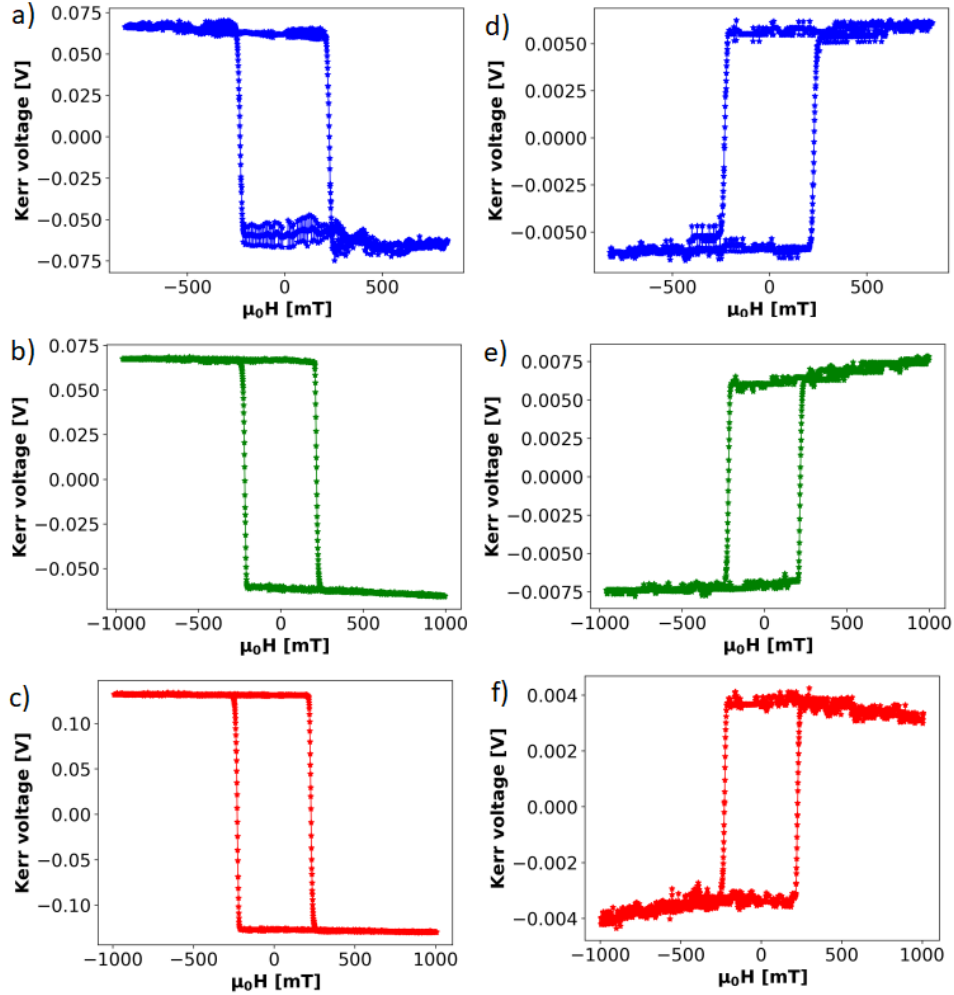


Figure 23: The hysteresis curves obtained for TbCo. (a)-(c) Hysteresis curves obtained with the  $2f$  signal at wavelengths: 408, 532, and 640 nm. (d)-(f) Hysteresis curves obtained from the  $1f$  signal at wavelengths: 408, 532, and 640 nm.

The hysteresis curves from the Ni samples with the  $2f$  signal are shown in Figure 24. The direction remains unchanged for these specific wavelengths, which shows that the sign of the Kerr rotation is the same. There is a small difference in shape between the curves obtained for Ni-150 and the other two Ni samples.

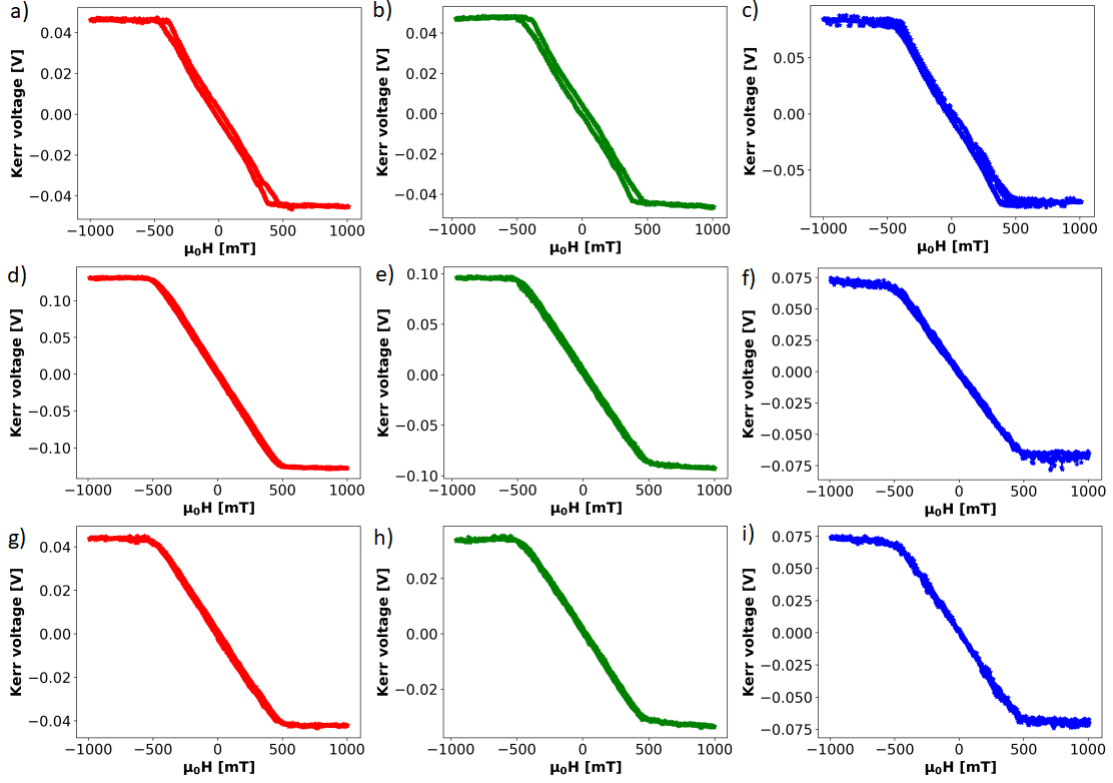


Figure 24: Hysteresis curves for the Ni samples with the  $2f$  signal. (a)-(c) Hysteresis curves obtained for Ni-150 at 408, 532 and 640 nm. (d)-(f) Hysteresis curves obtained for Ni-30 at 408, 532 and 640 nm. (g)-(i) Hysteresis curves obtained for Ni-24 at 408, 532 and 640 nm.

The hysteresis curves obtained with the  $1f$  signal for the Ni samples were in general noisy and due to this are only a few of them shown in Figure 25. There is a difference in direction for the curves obtained at 640 nm and the other two wavelengths, which is due to a difference in sign. This is consistent with the sign of the Kerr ellipticity for Ni in Figure 8.

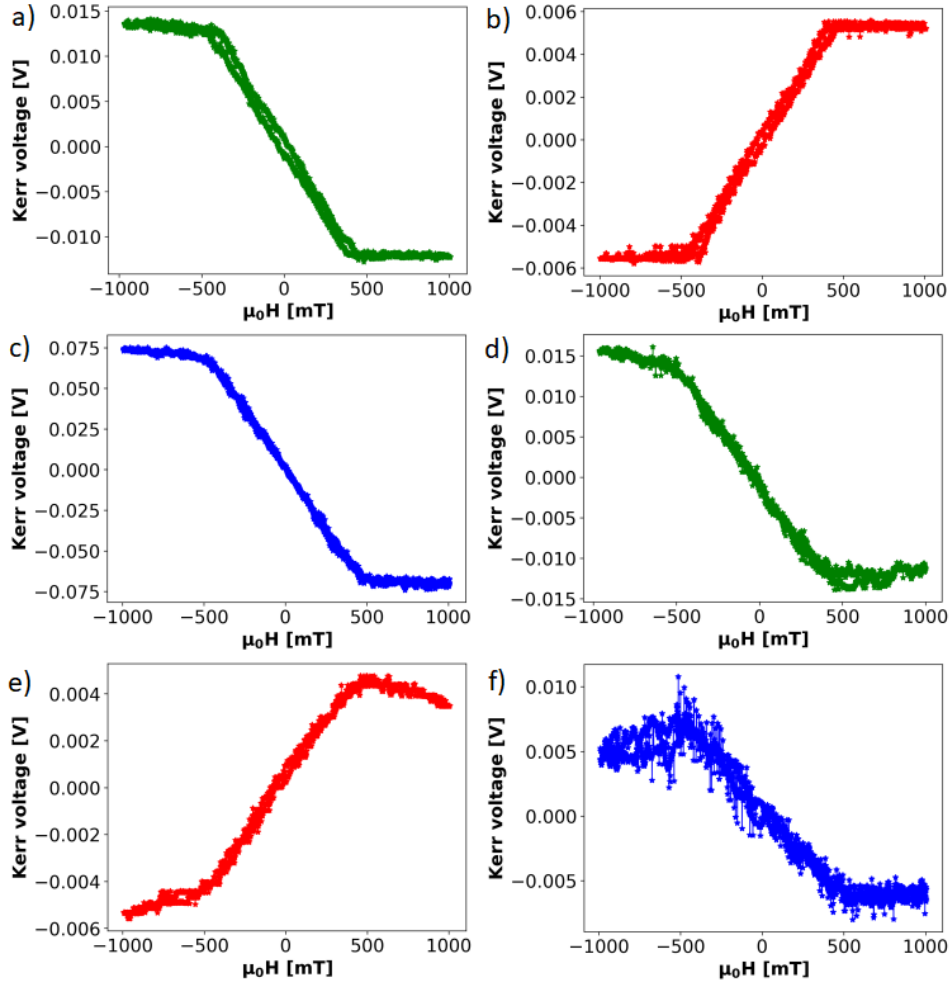


Figure 25: Hysteresis curves for the Ni samples with the  $1f$  signal. (a)-(b) Hysteresis curves obtained for Ni-150 at 532 and 640 nm. (c)-(e) Hysteresis curves obtained for Ni-24 at 408, 532 and 640 nm. (f) Hysteresis curve obtained for Ni-30 nm at 408 nm.

## 6 Discussion

### 6.1 Calibration and Kerr rotation

The determined calibration factors  $k_{rot}$  in Table 3 deviate considerably from the theoretical value, which from equation (11) is 46.915 deg. This is due to the presence of modulated interference, which introduces spurious signals into  $V_{1f}$  and  $V_{2f}$ . As a result, the values of  $\frac{V_{2f}}{V_{DC}}$  increased for the rotation angles  $\theta$ , which causes the value of  $k_{rot}$  to decrease. Additionally,  $k_{rot}$  displays a wavelength dependence. This is expected due to the wavelength-dependent behavior of the optical components. However, the differences in magnitude exceed the possible contribution from this. One reason for this could be the repositioning and adjustment of the optical components during the swap of lasers. This led to a variation in the tilt of the PEM, which has been shown to decrease modulated interference and the extent of this depends on the tilt angle [20]. As a result, the increase in  $V_{2f}$  varied for each wavelength. This can also explain the distinct difference in  $k_{rot}$  for the two calibrations performed at 640 nm. These were performed a couple of days apart and in this time period, the optical components had been moved around. The PEM was likely more tilted during the first calibration when  $k_{rot} = 40.205$  deg since it is closer to the literature value. It is important to add that  $k_{rot}$  remains unchanged during re-calibrations when all the components are fixed.

The Kerr rotations obtained from the two calibrations at 640 nm differ, as seen in Table 4. This suggests that the tilt of the PEM influences the obtained values. One possible explanation comes from the fact that tilting the PEM introduces polarization effects onto the transmitted beam [20]. The difference in tilt likely resulted in varying degrees of polarization effects. However, the nature and magnitude of these polarization effects are unknown [20]. The consequence of the polarization changes is that the values of  $\frac{V_{2f}}{V_{DC}}$  are mapped onto angles  $\theta$  that do not represent the actual polarization states. This error gets embedded into  $k_{rot}$ , which subsequently propagates into the Kerr rotation. Consequently, there are uncertainties in the validity of the determined values. It also follows that values obtained from different calibrations are not directly comparable, which severely limits the setup as it is not possible to compare measurements between wavelengths. However, it is possible to compare values from the same calibration. These uncertainties can be reduced in future measurements by ensuring that the light beam impinges onto the PEM at normal incidence to eliminate the introduced polarization effect. In addition, the PEM should be kept fixed during the swap of lasers to minimize the variations between calibrations. However, this is difficult to do in practice as the swap to the Coherent OBIS 532-20 laser required relocation of all optical components to ensure a proper beam path.

Figure 21 shows that the Kerr rotations obtained for the Ni samples differ distinctly, which indicates that the thickness of the film and the substrate material is of significance. This is due to interference effects, which occur in sufficiently thin samples. In these, the measured Kerr rotation consists of contributions from multiple reflections at the interfaces and therefore depends on the thickness and the refractive index of each layer [10]. If a sample is sufficiently thin depends on its properties as well as the laser intensity used. This could partially explain the deviation from the literature values as the Ni sample they used was thick enough to eliminate interference effect with respect to the light source they used [16].

The Kerr rotations obtained for TbCo differ significantly in magnitude and in sign compared to the literature values, as seen in Figure 22. This error in magnitude and sign might be due to the given composition on the sample container being incorrect. It has been shown that the sign of the Kerr angles in  $\text{Tb}_x\text{Co}_{100-x}$  depends on the composition [24]. Another contributing factor to the deviation in magnitude may be the difference in buffer and cap material as well as the variation in thickness of each layer. Further tests are required to find a clear explanation.

The obtained Kerr rotations with  $k_{rot}$  agree better with the literature values for the Ni samples compared to the Kerr rotations calculated with the theoretical value of 46.915 deg. This is shown in the Appendix. The explanation for this is that the calibration process captures the influence of modulated interference and other non-ideal behavior on  $\frac{V_{2f}}{V_{DC}}$  and maps it onto a polarizer angle  $\theta$ . Further, the hysteresis curves obtained with the  $1f$  signal show that changes in  $V_{1f}$  can be distinguished from noise introduced by modulated interference. This suggests that the Kerr ellipticity is measurable despite the presence of modulated interference by implementing the calibration process described previously.

## 6.2 Hysteresis curves

The results show that the experimental setup is capable of measuring hysteresis curves with both the  $1f$  and  $2f$  signals. These curves are more noisy as the wavelength decreases and this is because of the wavelength-dependent response of the Si detector. The presence of modulated interference does not affect the measurement of hysteresis curves because the contributions to  $V_{1f}$  and  $V_{2f}$  from spurious signals are independent of the magnetic field.

The process of measuring the hysteresis curves with the pre-written LabVIEW program is inefficient due to the inability to simultaneously measure the  $1f$  and  $2f$  signals. This process could be improved by writing a LabVIEW program that

measures  $V_{1f}$  and  $V_{2f}$  simultaneously. With this, it would be possible to produce hysteresis curves for the  $1f$  and  $2f$  signals from a single measurement.

### 6.3 Experimental set-up

There are several problems with the experimental setup in its current configuration, and all of these can be connected to the interaction between the light source, PEM, detector, and the sample.

The detector used displays a significant wavelength dependence in its response, making it unsuitable for measurements at shorter wavelengths, due to the need to increase the intensity. For our measurements, it was not possible to lower the intensity enough to eliminate interference effects because the detector was not sensitive enough. A more suitable detector for the experimental set-up would be a photomultiplier, as it offers higher sensitivity.

The presence of modulated interference and the problems with the calibration process can be removed by using a new light source with a tunable wavelength. This would make it possible to keep all the optical components in the setup fixed and ensure that the light beam strikes the PEM at normal incidence at all wavelengths. As a result, the calibration at each wavelength would be performed under identical conditions, which would make obtained values comparable. The first thing to consider for a new light source is the compatibility with the PEM. It should not be pulsed in such a way that it interacts with the modulation of the PEM. Secondly, modulated interference should not be present. This effect has only been observed when lasers are used in combination with the PEM [20]. However, it does not occur or is at least not noticeable for all lasers. An alternative is to use a white light source with a monochromator. The advantage of this is that there is no risk of modulated interference but it comes at the cost of having to introduce optical components to control the light beam. Lastly, it is important to be able to control the intensity of the light source to avoid interference effects by lowering the penetration depth of the light beam.

## 7 Conclusion

The aim of this project was to develop an experimental setup to perform spectroscopic MOKE measurements. The primary finding is that the experimental setup in its current configuration is not suitable for spectroscopic measurements, due to the inability to compare values obtained at different wavelengths. In order to facilitate this, a new light source with a tunable wavelength is required. However, the setup is capable of measuring hysteresis curves since the noise from modulated interference is independent of the applied magnetic field.

The calibration process for the Kerr rotation seems to work well as it captures the influence of non-ideal behaviour on  $\frac{V_{2f}}{V_{DC}}$  and maps it onto an angle  $\theta$ . However, the change of lasers introduced uncertainties during the calibration process. These can be reduced in future measurements by ensuring that the light beam strikes the PEM at normal incidence.

## 8 Future work

There are two clear priorities for continued work on the setup. The first is to find and implement a new light source with tunable wavelength. Secondly, the calibration process for the Kerr ellipticity has to be implemented. This would allow the setup to be used for spectroscopic measurement of the Kerr angles. Lastly, a new program to perform hysteresis measurement should be written, which simultaneously measures the  $1f$  and  $2f$  signals.

## 9 References

- [1] “Malus’ Law .” <https://sciencedemonstrations.fas.harvard.edu/presentations/malus-law>. Accessed: 2023/10/15.
- [2] A. K. Zvezdin and V. A. Kotov, *Modern Magnetooptics and Magnetooptical Materials*. Institute of Physics Publishing, 1997.
- [3] D. Floess and H. Giessen, “Nonreciprocal hybrid magnetoplasmonics,” *Reports on Progress in Physics*, vol. 81, p. 116401, oct 2018.
- [4] D. Chen, “Magneto-Optic Principles, Materials And Applications,” in *Electro-Optics Principles and Applications*, vol. 38, pp. 9–16, SPIE, 1973.
- [5] N. W. E. McGee, “The magneto-optical Kerr effect : theory, measurement and applications,” 1991.
- [6] D. A. Allwood, G. Xiong, M. D. Cooke, and R. P. Cowburn, “Magneto-optical Kerr effect analysis of magnetic nanostructures,” *Journal of Physics D: Applied Physics*, vol. 36, p. 2175, sep 2003.
- [7] S. Polisetty, J. Scheffler, S. Sahoo, Y. Wang, T. Mukherjee, X. He, and C. Binek, “Optimization of magneto-optical Kerr setup: Analyzing experimental assemblies using Jones matrix formalism,” *Review of Scientific Instruments*, vol. 79, 05 2008. 055107.
- [8] K. Légaré, V. Chardonnet, I. Bermúdez Macias, M. Hennes, R. Delaunay, P. Lassonde, F. Légaré, G. Lambert, E. Jal, and B. Vodungbo, “Analytic description and optimization of magneto-optical Kerr setups with photoelastic modulation,” *Review of Scientific Instruments*, vol. 93, 07 2022. 073001.
- [9] J. L. Erskine and E. A. Stern, “Magneto-optic Kerr Effect in Ni, Co, and Fe,” *Phys. Rev. Lett.*, vol. 30, pp. 1329–1332, Jun 1973.
- [10] A. Kimel, A. Zvezdin, S. Sharma, S. Shallcross, N. de Sousa, A. García-Martín, G. Salvan, J. Hamrle, O. Stejskal, J. McCord, S. Tacchi, G. Carlotti, P. Gambardella, G. Salis, M. Münzenberg, M. Schultze, V. Temnov, I. V. Bychkov, L. N. Kotov, N. Maccaferri, D. Ignatyeva, V. Belotelov, C. Donnelly, A. H. Rodriguez, I. Matsuda, T. Ruchon, M. Fanciulli, M. Sacchi, C. R. Du, H. Wang, N. P. Armitage, M. Schubert, V. Darakchieva, B. Liu, Z. Huang, B. Ding, A. Berger, and P. Vavassori, “The 2022 magneto-optics roadmap,” *Journal of Physics D: Applied Physics*, vol. 55, p. 463003, sep 2022.
- [11] K. Sato and T. Ishibashi, “Fundamentals of Magneto-Optical Spectroscopy,” *Frontiers in Physics*, vol. 10, 2022.

- [12] J. F. Schmidt, “Time dependent and energy resolved measurement on magnetic films,” 2008.
- [13] E. Hecht, *Optics*. Pearson, 2017.
- [14] D. S. Kliger, J. W. Lewis, and C. E. Randall, *Polarized Light in Optics and Spectroscopy*. Academic Press, 1990.
- [15] C. Rizal, H. Shimizu, and J. R. Mejía-Salazar, “Magneto-Optics Effects: New Trends and Future Prospects for Technological Developments,” *Magnetochemistry*, vol. 8, no. 9, 2022.
- [16] S. Visnovsky, V. Parizek, M. Nyvlt, P. Kielar, V. Prosser, and R. Krishnan, “Magneto-optical Kerr spectra of nickel,” *Journal of Magnetism and Magnetic Materials*, vol. 127, no. 1, pp. 135–139, 1993.
- [17] P. Oppeneer, “Chapter 3 Magneto-optical Kerr spectra,” vol. 13 of *Handbook of Magnetic Materials*, pp. 229–422, Elsevier, 2001.
- [18] S. Sugano and N. Kojima, *Magneto-Optics*, vol. 128. Springer Science & Business Media, 2013.
- [19] “Manual MODEL SR830 DSP Lock-In Amplifier.” <https://www.thinksrs.com/downloads/pdfs/manuals/SR830m.pdf>. Accessed: 2023/06/13.
- [20] T. C. Oakberg, “Modulated interference effects: use of photoelastic modulators with lasers,” *Optical Engineering*, vol. 34, no. 6, pp. 1545–1550, 1995.
- [21] P. S. Theocaris and E. E. Gdoutos, *Matrix Theory of Photoelasticity*, vol. 11. Springer, 2013.
- [22] “PEM Principles Of Operation.” <https://www.hindsinstruments.com/knowledge-center/technology-primer/pem-photoelastic-modulation/principles-of-operation/>. Accessed: 2023/05/31.
- [23] T. C. Oakberg, “Magneto-optic Kerr Effect,” *Hinds Instruments*, vol. 1, no. 1, 2005.
- [24] A. Ciuciulkaite, K. Mishra, M. V. Moro, I.-A. Chioar, R. M. Rowan-Robinson, S. Parchenko, A. Kleibert, B. Lindgren, G. Andersson, C. S. Davies, A. Kimel, M. Berritta, P. M. Oppeneer, A. Kirilyuk, and V. Kapaklis, “Magnetic and all-optical switching properties of amorphous  $Tb_xCo_{100-x}$  alloys,” *Phys. Rev. Mater.*, vol. 4, p. 104418, Oct 2020.

- [25] “DET100A2 Large Area Si Biased Detector User Guide.” <https://www.thorlabs.com/thorproduct.cfm?partnumber=DET100A2#ad-image-0>. Accessed: 2023/06/13.

## 10 Appendix

### Response of Thorlabs DET100M at different wavelengths

The responsivity of the Thorlabs DET100M Si detector is shown in Figure 26.

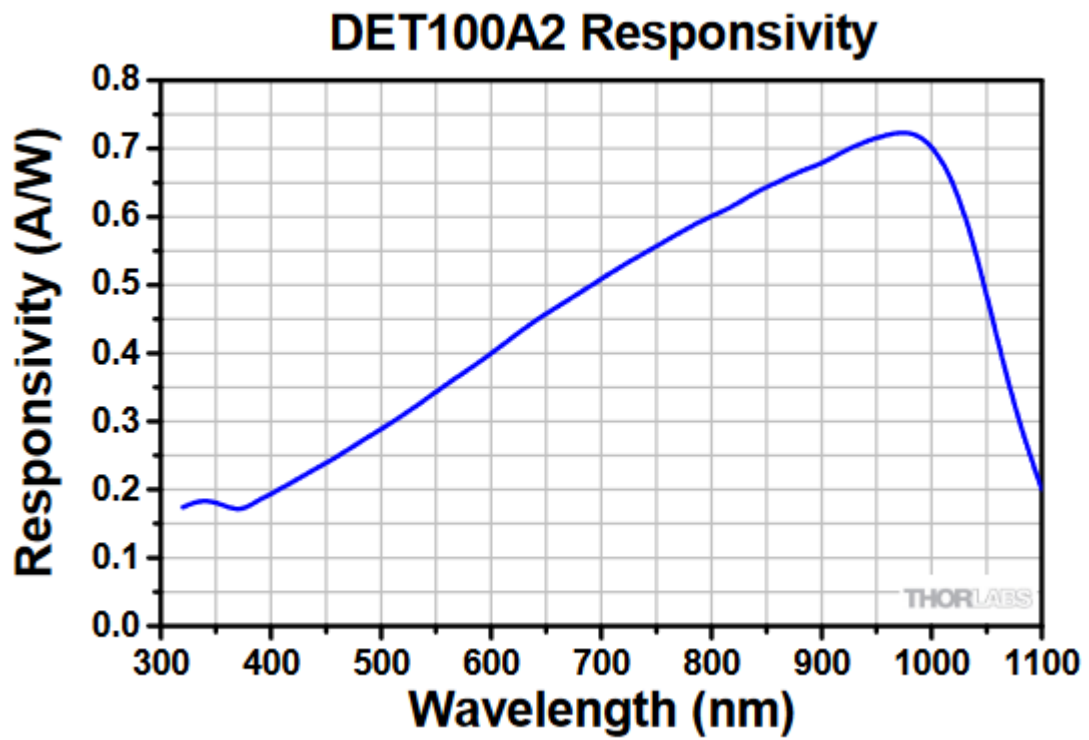


Figure 26: The responsivity of the Thorlabs DET100M Si detector [25].

## Kerr rotations

Table 5: Kerr rotations determined with the theoretical value of  $k_{rot}$  and the value of  $k_{rot}$  from the calibration at 640 nm. The literature value of Ni is  $\approx -0.142$  deg.

	Kerr rotation [deg]		
	Ni-24	Ni-30	Ni-150
$k_{theo} = 46.915$	$0.234 \pm 0.002$	$0.301 \pm 0.002$	$0.223 \pm 0.002$
$k_{rot} = 32.507$	$-0.162 \pm 0.001$	$-0.209 \pm 0.002$	$-0.154 \pm 0.002$

Table 6: Kerr rotations determined with the theoretical value of  $k_{rot}$  and the value of  $k_{rot}$  from the calibration at 640 nm. The literature value of Ni is  $\approx -0.142$  deg.

	Kerr rotation [deg]		
	Ni-24	Ni-30	Ni-150
$k_{theo} = 46.915$	$0.185 \pm 0.009$	$0.270 \pm 0.003$	$0.175 \pm 0.004$
$k_{rot} = 40.205$	$0.159 \pm 0.008$	$0.231 \pm 0.002$	$0.150 \pm 0.003$

Table 7: Kerr rotations determined with the theoretical value of  $k_{rot}$  and the value of  $k_{rot}$  from the calibration at 532 nm. The literature value of Ni is  $\approx -0.131$  deg.

	Kerr rotation [deg]		
	Ni-24	Ni-30	Ni-150
$k_{theo} = 46.915$	$0.222 \pm 0.002$	$0.315 \pm 0.002$	$0.260 \pm 0.003$
$k_{rot} = 28.172$	$0.133 \pm 0.001$	$0.189 \pm 0.001$	$0.156 \pm 0.002$

Table 8: Kerr rotations determined with the theoretical value of  $k_{rot}$  and the value of  $k_{rot}$  from the calibration at 408 nm. The literature value of Ni is  $\approx -0.162$  deg.

	Kerr rotation [deg]		
	Ni-24	Ni-30	Ni-150
$k_{theo} = 46.915$	$0.269 \pm 0.013$	$0.317 \pm 0.029$	$0.414 \pm 0.015$
$k_{rot} = 21.041$	$0.121 \pm 0.006$	$0.142 \pm 0.013$	$0.185 \pm 0.007$